Electronic Supplementary Material (ESI) for Chemical Communications.

SUPPORTING INFORMATION

Guanidinium substitution-dependent phase transitions, ionic conductivity and dielectric properties of $MAPbI_3$

F. B. Minussi[1], E. M. Bertoletti[1], S. P. Reis[2], J. F. Carvalho[3], E. B. Araújo[1]

[1] Department of Physics and Chemistry, São Paulo State University, 15385-000 Ilha Solteira, Brazil

[2] Federal Institute of Education, Science and Technology of São Paulo, 15503-110 Votuporanga, Brazil

[3] Institute of Physics, Federal University of Goiás, 74690-900 Goiânia, Brazil

Supplementary Note 1: Materials and methods

Five compositions of the $GA_xMA_{1-x}PbI_3$ system were chosen, for x ranging from 0.0 to 0.4. Amounts of PbI_2 (Sigma-Aldrich, 211168, 99%), MAI (Sigma-Aldrich, 793493, 98%), and GAI (Sigma-Aldrich, 806056, 99%), precursors were weighted in the desired proportions of each composition and dissolved to 0.75 $mol.l^{-1}$ solutions in a mixture consisting in 70%v. of DMF (Sigma Aldrich, 227056, 99.8%) and 30%v. of DMSO (Sigma Aldrich, 276855, 99.9%). The solutions were stirred at ~ 30 °C for 2 hours and then slowly evaporated at 70 - 80 °C for ~ 10 hours under magnetic stirring in dark conditions. The remaining yellowish mixtures were dried in an oven at 80 - 90 °C for ~ 11 hours, resulting in approximately 1.7 g dark, blackish powders. The powders were ground, sieved in a 250 μm aperture sieve (60 mesh), and kept in a sealed flask with PVC film in a desiccator. 200 - 250 mg of the powders were uniformly spread into a 13 mm diameter circular cavity of a metallic mold and compacted with a pressure of approximately 220 MPa to produce $GA_xMA_{1-x}PbI_3$ pellets, as shown in Fig. S1. Lastly, the pellets were sintered in an electric furnace at 120 °C for 2 hours and slowly cooled to room temperature inside the furnace. Estimations using energy-dispersive X-ray analysis using Oxford Instruments INCA x-act equipment show I/Pb molar ratios of about 2.9 to 3.1 (Table S1), thus, in very good agreement with the theoretical value of 3.

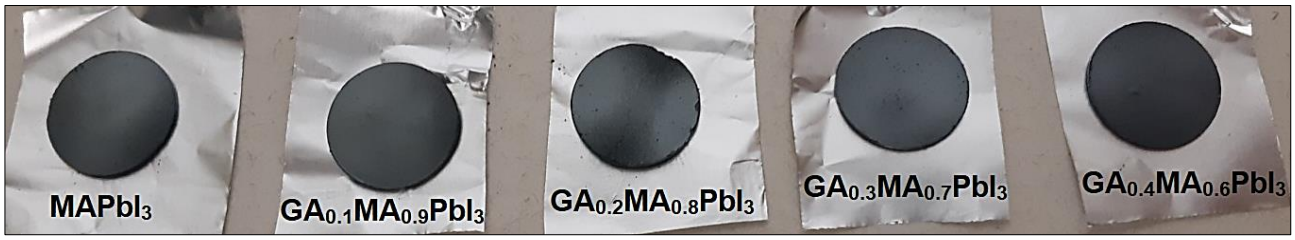

Fig. S1 - Examples of $GA_xMA_{1-x}PbI_3$ sintered pellets.

Table S1 - Carbon, nitrogen, iodine and lead mass content for each $GA_xMA_{1-x}PbI_3$ composition and the calculated iodide to lead molar ratio. Estimations based on EDX analyses of 500x magnified regions.

Composition	C mass %	N mass %	I mass %	Pb mass %	I/Pb molar ratio
$MAPbI_3$	3.42 ± 0.57	2.10 ± 0.63	61.81 ± 0.72	32.67 ± 0.58	3.09 ± 0.07
$GA_{0.1}MA_{0.9}PbI_3$	4.13 ± 0.54	2.64 ± 0.63	60.07 ± 0.66	33.16 ± 0.53	2.96 ± 0.06
$GA_{0.2}MA_{0.8}PbI_3$	3.06 ± 0.54	2.42 ± 0.60	60.53 ± 0.68	33.98 ± 0.55	2.91 ± 0.06
$GA_{0.3}MA_{0.7}PbI_3$	2.67 ± 0.55	2.89 ± 0.62	60.95 ± 0.68	33.49 ± 0.55	2.97 ± 0.06
$GA_{0.4}MA_{0.6}PbI_3$	3.15 ± 0.55	3.90 ± 0.64	59.33 ± 0.68	33.62 ± 0.55	2.88 ± 0.06

X-ray diffraction (XRD) analyses were performed using a Rigaku Ultima IV diffractometer with CuK_α radiation (λ = 1.5406 Å), under 40 kV and 20 mA, in continuous scan (2° min^{-1}) mode, in the range of 2θ from 10 to 60°. High definition XRD data were collected in a Bruker D8 Discover

diffractometer using $CuK_{\alpha 1}$ radiation from a Johansson monochromator attached to an X-ray tube with cooper anode, in step scan (step size of 0.02°) mode, in the range of 2θ from 5 to 80°, using a linear detector, with integration times of 260 s on a 3.6° range (steps of 0.010522° between readings). Temperature-dependent XRD analyses were performed using a Bruker D8 Discover diffractometer, with CuK_{α} radiation under 40 kV and 40 mA. The sample was mounted in a specific sample holder, coupled to a Materials Research Instrument temperature chamber system, and acquired in the 2θ interval from 27 to 29.5°, with 0.02° step, at heating temperatures of 143 K to 343 K (10 K step) in a vacuum atmosphere. Microstructure images of the samples were obtained in a Zeiss EVO LS15 scanning electron microscope (SEM), with a tungsten beam, operating in the voltage range between 10 and 20 kV, by secondary electron analysis. From this point forward, measurements were carried out at room temperature (295 - 300 K) in the cases that were not stated.

For electrical measurements, a matrix of 10 × 10 circular gold electrodes of about 0.65 mm diameter (SEM measured) were sputtered on top of $GA_xMA_{1-x}PbI_3$ sintered pellets using a shadow mask, while a bottom gold electrode was deposited over the entire sample surface. The dielectric (impedance) measurements were performed in a Displex ARS CSW-202 closed system using an Agilent 4284A LCR meter to collect conductance (G) and susceptance (B) measurements in the frequency (f) 6×10^2 to 10^6 Hz and temperature 100 to 380 K ranges under 0.3 K min^{-1} heating rate. All electrical measurements were carried out in vacuum and in the dark to avoid external effects. For data analysis, the recorded G and B measurements were treated in terms of complex impedance ($Z^* = Z' - iZ''$) and complex dielectric permittivity ($\varepsilon^* = \varepsilon' + i\varepsilon''$). The values of the important components used in this study were calculated using the relations

$$Z' = \frac{G}{B^2 + G^2}$$

$$Z'' = \frac{G}{B^2 + G^2}$$

$$\varepsilon' = \frac{B}{\omega C_0}$$

where $\omega = 2\pi f$ is the angular frequency and $C_0 = \varepsilon_0 a/d$, where ε_0 is the permittivity of free space, a is the electrode area, and d is the sample thickness. In the present study, $a = 347\ \text{nm}^2$ for all samples, and their thicknesses were different, as indicated in Fig. S15.

Supplementary Note 2: General structure characterization

From the XRD profiles in Fig. S2, a clear formation of perovskite phases is observed for all of our $GA_xMA_{1-x}PbI_3$ compositions. Importantly, the typical PbI_2 peak at ~11° is essentially inexistent, except for a very small one for x = 0.2. At the x = 0.3 and x = 0.4 compositions, we see new peaks in the diffractograms, which coincide with the diffraction pattern of the hexagonal structure of $GAPbI_3$. Indeed, the literature indicates that the solubility limit of GA in the host $MAPbI_3$ is reached at about 25 molar percent (x = 0.25) [1]. Therefore, we expect this same behavior for our samples.

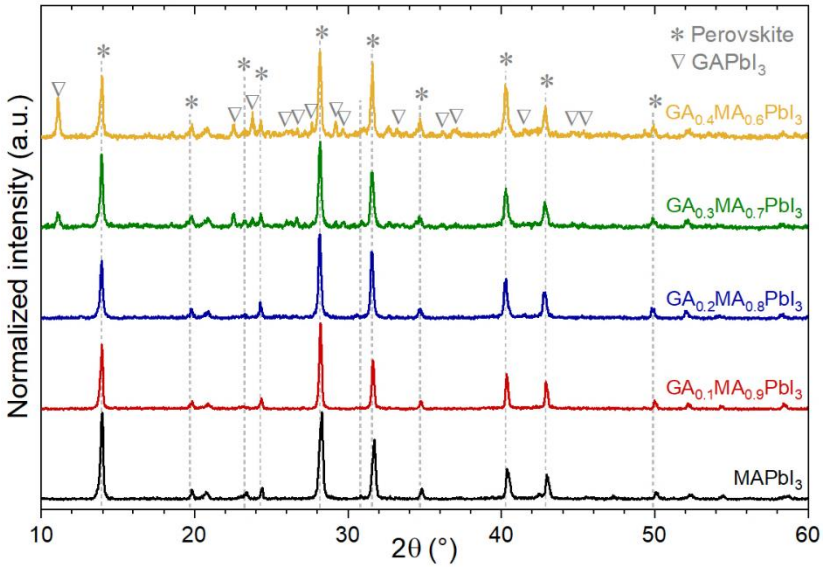

Fig. S2 - Diffractograms of sintered $GA_xMA_{1-x}PbI_3$ pellets.

From a microstructural standpoint (Fig. S3), the sintering process led to high densification degrees and well-formed grains, with sizes ranging approximately from 0.5 to 1 μm. Noteworthy, elongated structures appeared for the x = 0.3 and x = 0.4 compositions. These structures are similar to stripe-like GA-containing lead iodide crystallites formed by slow cooling in solution [2] and rod-like regions present in $GA_xMA_{1-x}PbI_3$ films for x of 0.3 or above [1], confirming the segregation of $GAPbI_3$ phase in these compositions.

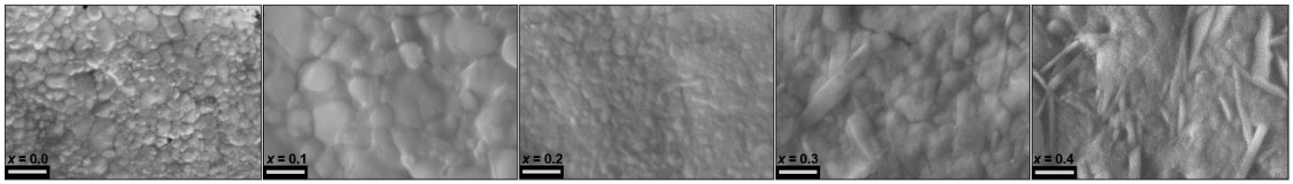

Fig. S3 - Representative SEM microstructure images of $GA_xMA_{1-x}PbI_3$ pellets. Scale bar: 1 μm.

Overall, the above results indicate good quality of the samples and that the synthesis procedure led to the desired materials, with properties within the expected. To exclude secondary phase effects,

we did not perform further analyses in the x = 0.3 and x = 0.4 compositions. In Fig. S4 are shown the high-definition diffractograms of $MAPbI_3$, $GA_{0.1}MA_{0.9}PbI_3$ and $GA_{0.2}MA_{0.8}PbI_3$ in the important regions to differentiate the tetragonal and cubic structures between these compositions.

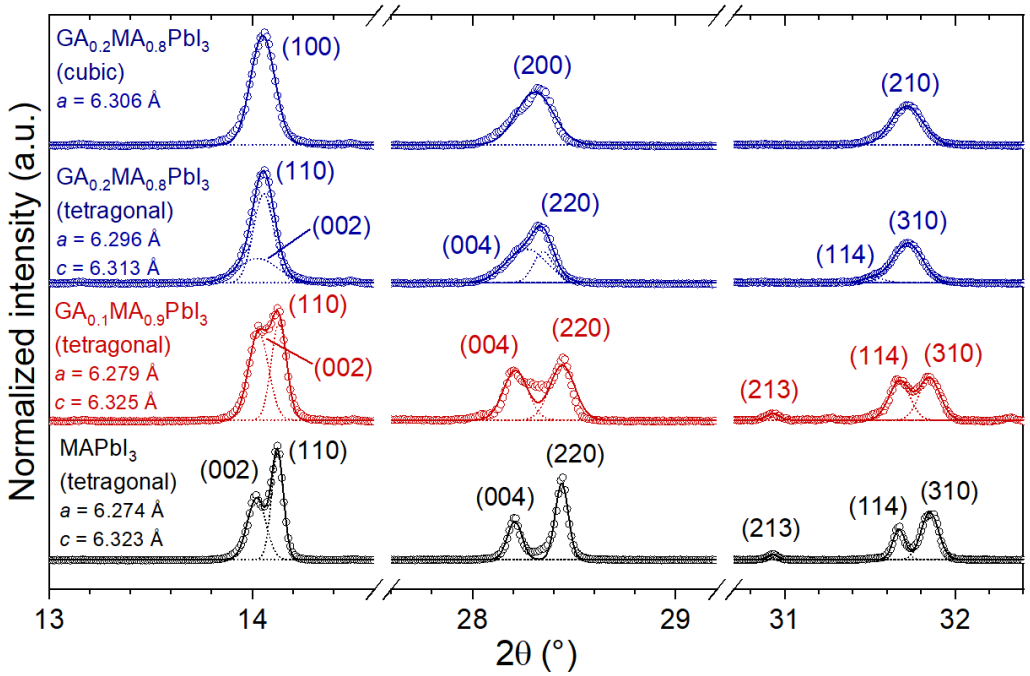

Fig. S4 - High-definition X-ray diffraction profiles of $GA_xMA_{1-x}PbI_3$ polycrystals at room temperature. Only the regions of main peaks are shown. Plane attributions are due to the $I4cm$ and $Pm\bar{3}m$ space groups typically reported for tetragonal and cubic $MAPbI_3$-based structures, respectively. Lattice parameters given for tetragonal diffraction patterns are the pseudo-cubic ones.

As can be seen, the diffraction peak assigned to cubic (200) in $GA_{0.2}MA_{0.8}PbI_3$ is clearly non-Gaussian, leaving the possibility that it is a peak attributed to the superposition of tetragonal (004) and (220) diffraction peaks. On the other hand, the peaks assigned as (100) and (210) do seem close to a single peak. Also, the peak assigned as tetragonal (213) structure disappears. These results shade doubt on the correct structure. When the lattice parameters are calculated, a difference of only 0.27% between a and c for $GA_{0.2}MA_{0.8}PbI_3$ taken as tetragonal is noticed. Taking the results all together, we speculate that the inference of a structure for higher GA^+ content compositions is rather difficult because of a continuous transition between two very similar structures. This speculation is corroborated by two main facts. First, the reported coexistence of tetragonal and cubic phases in pure $MAPbI_3$ in the vicinity of the phase transition, as the transition is known to occur continuously rather than abruptly. Second, the reduced tetragonality factor with increasing GA^+ content, as discussed in the Supplementary Note 6. Also, one has to consider that the differences in XRD data between tetragonal and cubic perovskites are very subtle, leading to somewhat diffuse interpretations. Overall, the results were dubious enough to motivate us to search for a possible change in the tetragonal-to-cubic phase transition with the GA^+ content.

Supplementary Note 3: DSC analysis

To gain greater cohesion on the transition temperatures obtained from temperature-dependent XRD analysis in the main text, we performed differential scanning calorimetry (DSC) experiments. Thermograms (Fig. S5) were obtained using a Netzsch DSC 204 F1 Nevio equipment using about 2 mg fragments of sintered pellets. Measurements were performed from 193 K to 373 K (5 minutes with the constant temperature at 193 K), using a heating rate of 10 K min^{-1}, aluminum crucibles (40 µl), and a 50 ml min^{-1} nitrogen flow. Despite the not optimal baselines, we could extract reasonable transition temperatures related to endothermic peaks in each composition. The comparison between DSC and XRD results is given in Table S2. We see a good correspondence of both results. As a demonstration of the feasibility of our results, we calculated a transition enthalpy of 1.84 kJ mol^{-1} for our $MAPbI_3$, close to the reported value of 2.58 kJ mol^{-1} [3].

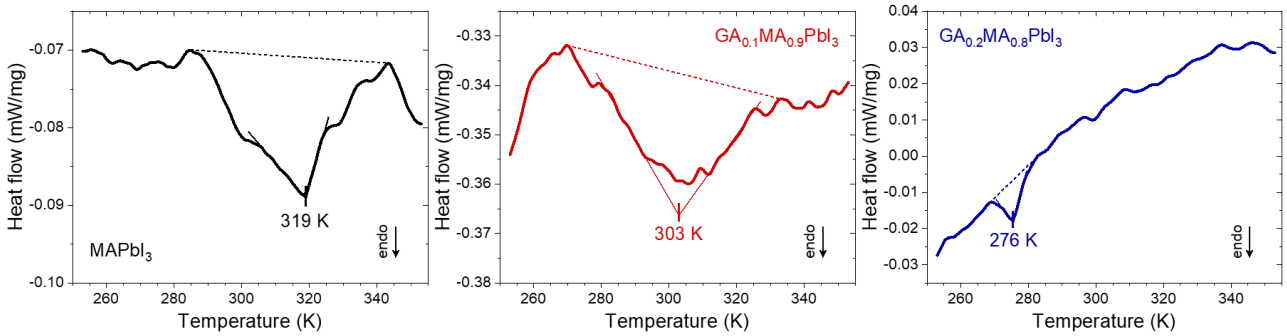

Fig. S5 - DSC curves (thick lines) and respective segments (thin lines) used for estimation of transition temperatures. Dashed lines are tentative baselines.

Table S2 - Comparative summary of DSC and XRD results on the estimated tetragonal-to-cubic transition temperatures. XRD values refer to Fig. 1(a) transition ranges in the main text.

Composition	$T_{\beta\rightarrow\alpha}$ **(K)**	
	DSC	**XRD**
$MAPbI_3$	319	323 - 333
$GA_{0.1}MA_{0.9}PbI_3$	303	303 - 313
$GA_{0.2}MA_{0.8}PbI_3$	276	273 - 283

Supplementary Note 4: Some literature observations regarding GA^+ addition

Kubicki et al. [4] reported an interesting trend on the charge carrier lifetimes, with decay constants of approximately 0.081, 0.935, 3.1, and 0.369 μs for $MAPbI_3$, $GA_{0.05}MA_{0.95}PbI_3$, $GA_{0.10}MA_{0.90}PbI_3$, and $GA_{0.25}MA_{0.75}PbI_3$, respectively. A possible explanation was that the substitution of MA^+ by GA^+ may initially lead to stabilization, but with higher GA^+ contents, the lattice would experience additional strain that negatively affects the charge carrier stability. Even though it seems to be a good explanation, we also speculate that if measurements are carried under room temperature, the increasing GA^+ content would also cause the transition from a tetragonal to cubic structure, contributing to a change on the expected behavior of increasing decay constants with GA^+. In their XRD data (provided in the supplementary material), we observe that the peak splitting feature vanishes when GA^+ is increased from 20 to 25% and also an apparent disappearance of the peak at ~ 31°, perhaps suggesting the proposed transition. Based on that same idea, we argue that the following other "anomalies" may also be connected to the GA^+-induced phase transition.

a) A sudden drop on the calculated c lattice parameter from $GA_{0.10}MA_{0.90}PbI_3$ to $GA_{0.15}MA_{0.85}PbI_3$ based on a tetragonal $I4cm$ space group [5].
b) In a $GA_x(CsFAMA)_{1-x}$ system, the addition of GA^+ up to $x = 0.10$ leads to an increase in PL decay times and peak energy position, followed by a reduction in both parameters for higher GA^+ contents [6].
c) Average carrier lifetimes and PL intensities are maximum at $x = 0.15$ in $GA_xMA_{1-x}PbI_3$ films with x up to 0.30. A steep decrease on the (112) diffraction peak intensity for x higher than 0.15 [7].

Supplementary Note 5: Gaussian fits of temperature-dependent XRD data

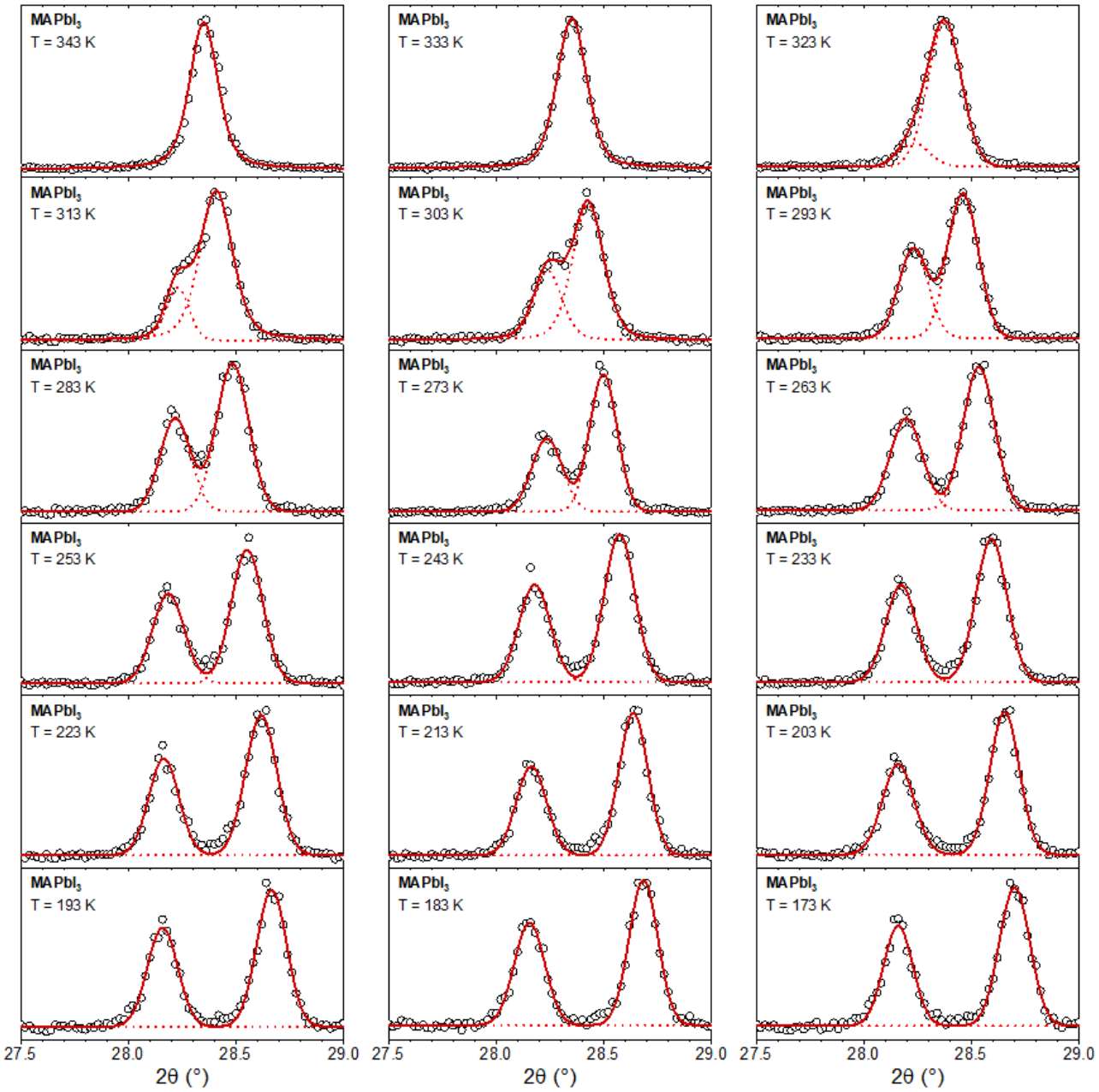

Fig. S6 - Gaussian fits of $MAPbI_3$ temperature-dependent XRD data. Black hollow circles are experimental data. Dashed red lines are the Gaussians of each peak, whereas the continuous red lines are the cumulative curves.

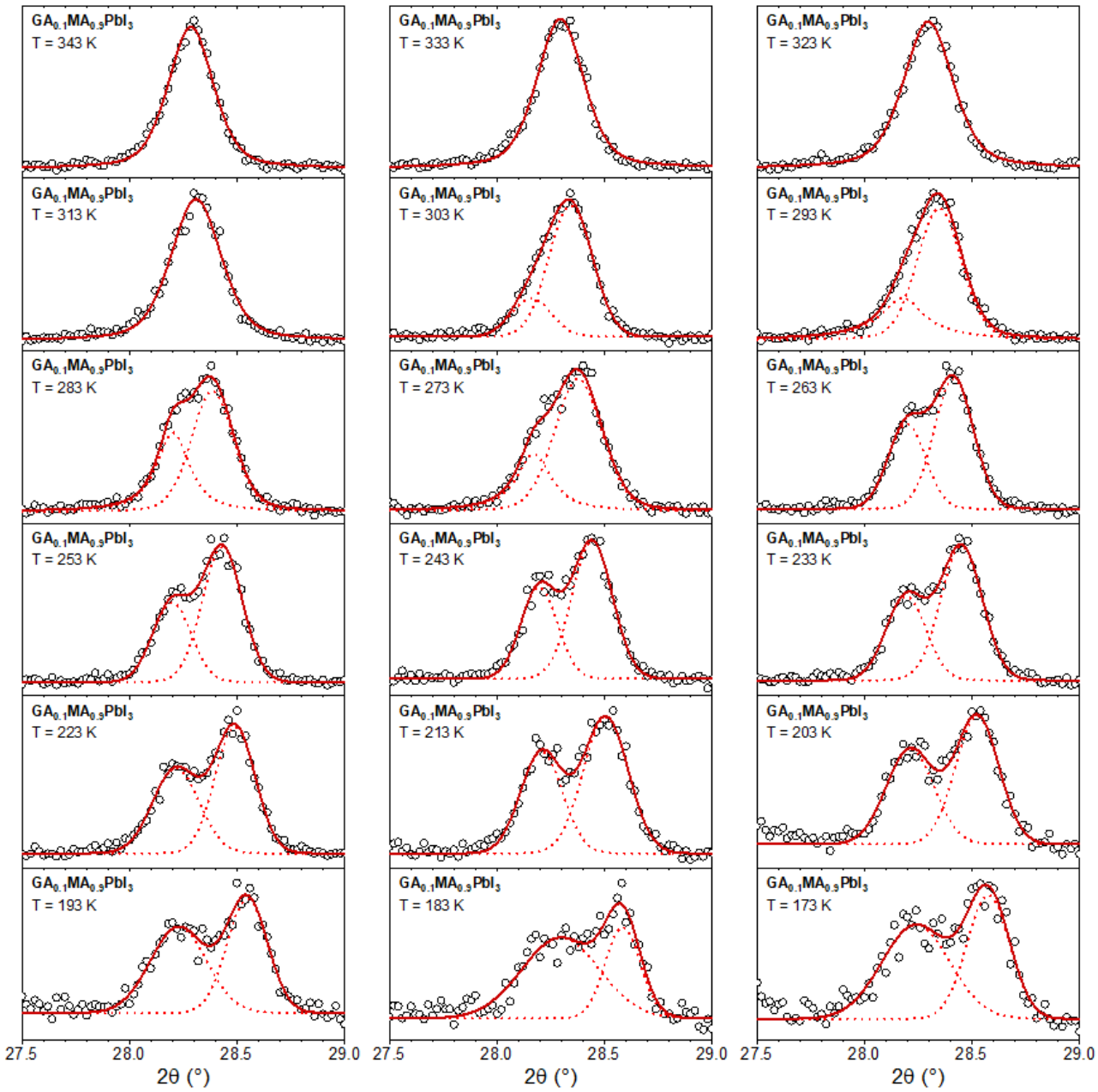

Fig. S7 - Gaussian fits of $GA_{0.1}MA_{0.9}PbI_3$ temperature-dependent XRD data. Black hollow circles are experimental data. Dashed red lines are the Gaussians of each peak, whereas the continuous red lines are the cumulative curves.

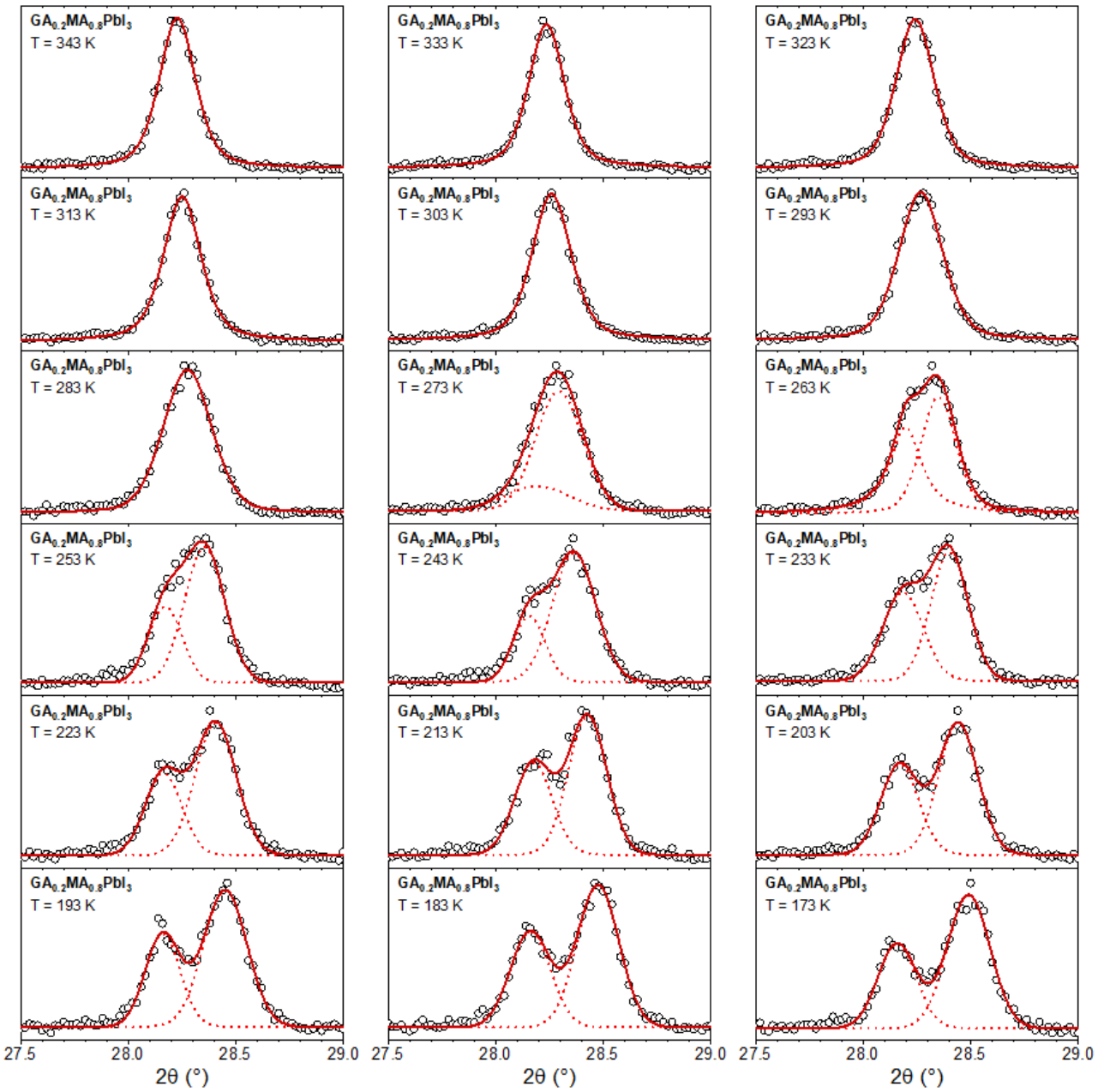

Fig. S8 - Gaussian fits of $GA_{0.2}MA_{0.8}PbI_3$ temperature-dependent XRD data. Black hollow circles are experimental data. Dashed red lines are the Gaussians of each peak, whereas the continuous red lines are the cumulative curves.

Supplementary Note 6: Temperature-dependent crystal properties

Fig. S9 shows the variation of tetragonality factor and cell volume with temperature. The tetragonality factor shows a clear decreasing trend with the guanidinium content, suggesting that GA^+ incorporation leads to a higher structural similarity between tetragonal and cubic phases. From enthalpy of mixing arguments, it was suggested that $GA_xMA_{1-x}PbI_3$ mixed perovskites might have a structure close to cubic [8], on par with our speculation. We believe that this is likely related to the decreased transition temperature with increasing GA^+ content.

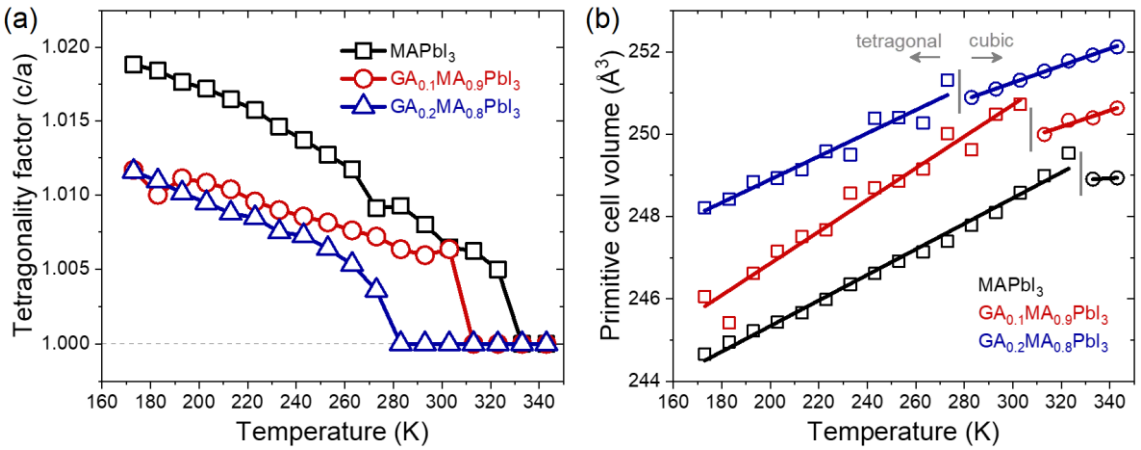

Fig. S9 – a) Tetragonality factor and b) cell volume as a function of temperature. Data in the tetragonal phase were calculated using pseudo-cubic parameters. Lines in volume versus temperature are linear fits to experimental data.

As for the cell volume, we obtained the expected increase with GA^+ content due to its higher effective radius than MA^+. With the volume data, we estimated volumetric thermal expansion coefficients (α_V) for both tetragonal and cubic phases from the linear fits of Fig. S9. Results are summarized in Table S3, which also presents a comparison with literature data. A complete comparison is given in [9].

Table S3 - Calculated volumetric thermal expansion coefficients and comparison with a few literature results on similar materials.

Composition	α_V (10^{-5} K^{-1})		Reference
	Tetragonal	Cubic	
$MAPbI_3$	13	-	
$GA_{0.1}MA_{0.9}PbI_3$	16	7.9	Present work
$GA_{0.2}MA_{0.8}PbI_3$	11	8.3	
$MAPbI_3$	15.7		[10]
$MAPbI_3$	4.2 (linear)	3.5 (linear)	[11]
$FAPbI_3$	~20	~10	[12]
$FA_{0.5}MA_{0.5}PbI_3$		22	[13]

The obtained values are within the reported in other works. Our results demonstrate that the incorporation of guanidinium affects the thermal expansion coefficient. By itself, this can be an interesting factor because it makes it possible to control the mismatch between expansions and contractions under operational conditions between the absorbing layer and the other layers of a device. Another curious result is the approximation of the expansion coefficients between the tetragonal and cubic structures with the increase of the guanidinium content. It potentially decreases the thermal stresses that would inevitably occur during thermal variations on device operation. Also, it serves as corroboration to the proposed higher similarity between tetragonal and cubic phases with increasing guanidinium content. Noteworthy to mention the curious result of the thermal expansion coefficient of $GA_{0.2}MA_{0.8}PbI_3$ being lower than that of $MAPbI_3$. A similar result was obtained from DFT calculations, showing that $GA_{0.25}MA_{0.75}PbI_3$ has a lower thermal expansion coefficient than $MAPbI_3$, associated with the former's stiffer structure [14].

Supplementary Note 7: Dielectric permittivities

Understanding the dielectric properties is essential to understand possible relationships with the other properties observed for its crystals and devices. Furthermore, together with systems such as $FA_xMA_{1-x}PbI_3$ [15] and $DMA_xMA_{1-x}PbI_3$ [16], it advances the possibility of generalization and prediction of dielectric properties of mixed organic cation systems.

In addition to the electronic contribution associated with the displacement of the electronic clouds of atoms and ions that constitute the material, the intrinsic electrical polarization of $MAPbI_3$ is derived from main contributions, namely, due to the ionic polarization resulting from the displacement of Pb^{2+} in the PbI_6 octahedron [17], ionic polarization associated with the displacement of MA^+ cations concerning the negative center of PbI_3^- and orientation (dipolar) polarization of the dipole of the MA^+ cation [18]. These mechanisms have relaxation times on the order of femtoseconds for electronic polarization, picoseconds for ionic polarization, and nanoseconds for dipolar polarization [19]. On the other hand, the contribution by space charges, associated with the redistribution of charged species by the structure, such as ions, have relaxation times in the order of microseconds to seconds [20]. The phenomenon called dielectric relaxation is the change of the electric polarization after applying an electric field to a sample [21]. After applying such an electric field, the time needed for a given polarization mechanism to relax to its ground state is associated with the so-called relaxation time. When the alternation time of an electric field is less than the relaxation time of a particular polarization mechanism, this mechanism vanishes in the sense that it is no more contributing to the material's polarization. This process is accompanied by a decrease in the dielectric permittivity when the frequency is increased. In the frequency range studied here, this drop is mostly associated with the relaxation of space charges of the contributions to the material's polarization. In Fig. S10 are given the dispersion curves of relative dielectric permittivity (ε') at different temperatures of $GA_xMA_{1-x}PbI_3$ perovskites.

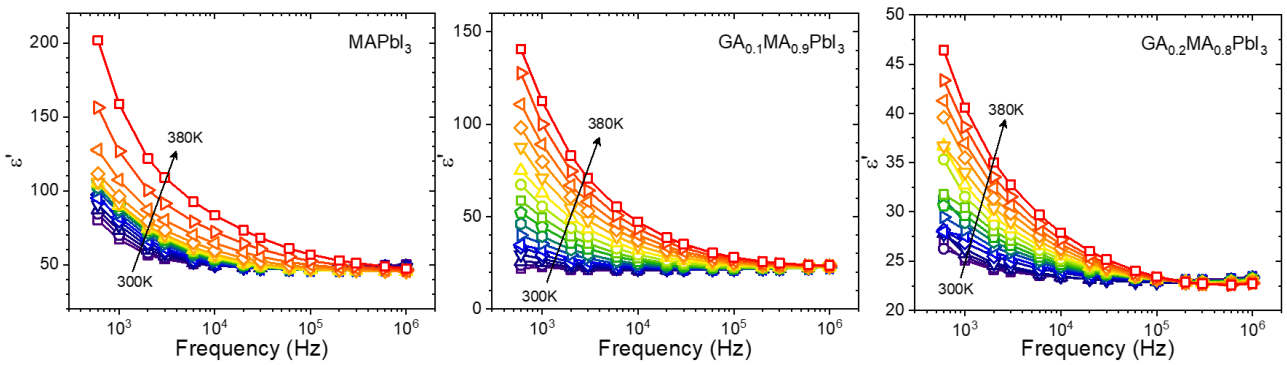

Fig. S10 - Relative dielectric permittivity dispersion of $GA_xMA_{1-x}PbI_3$ perovskites in the 600 Hz to 1 MHz and 300 to 380 K ranges. Lines are guides to the eyes.

We observe the typical dielectric relaxation behavior for the dielectric permittivity. Importantly, the introduction of GA^+ cations into the $MAPbI_3$ lattice dramatically reduces the permittivities dispersion, implying lower ionic conductivity contributions. That means one can expect that the formation of GA-MA solid solutions reduces the ionic conductivity, which is indeed obtained for the studied materials (a detailed discussion is given in Supplementary Note 8). Hence, we expect that the ac characteristics are dominated by progressively lower range migration as we increase GA^+ content, a mechanism which recently has been suggested to inhibit photoinduced phase segregation [22]. From the relative permittivity dispersion, we can obtain the intrinsic contributions to ε' operating in a given frequency range by taking the high-frequency limit. This contribution, sometimes termed as ε_∞, is correspondent to the intrinsic dielectric polarization in bulk and can be reasonably estimated in our results by simply taking the 1 MHz value of ε' at a given temperature since our plateaus are quite large. These values are important for the calculation of relaxation times, also in Supplementary Note 8.

Supplementary Note 8: Calculation of conductivities and relaxation times

The properties studied from the analysis of impedance spectroscopy data are those for which the corresponding physical processes occur at the frequencies (time scales) of the applied alternating voltage (electric field). An important feature for such analysis is the observation of a peak in the impedance data. This peak is related to the relaxation frequency of a given process and can be estimated by observing the peak frequency in a plot of the dispersion of the imaginary part of the impedance (Z''). However, as shown in Fig. S11, this peak is not visible at several (low) temperatures in the studied frequency range, which prevents its simple graphic determination. However, it can be obtained mathematically by associating the impedance data with an equivalent circuit model, which represents the electrical response of the material. To model the impedance data, we can use the Cole-Cole relaxation model [23]. An associated equivalent circuit is given in Fig. S12. It is noteworthy that this model was already applied to a mixed-cation lead iodide perovskite [16].

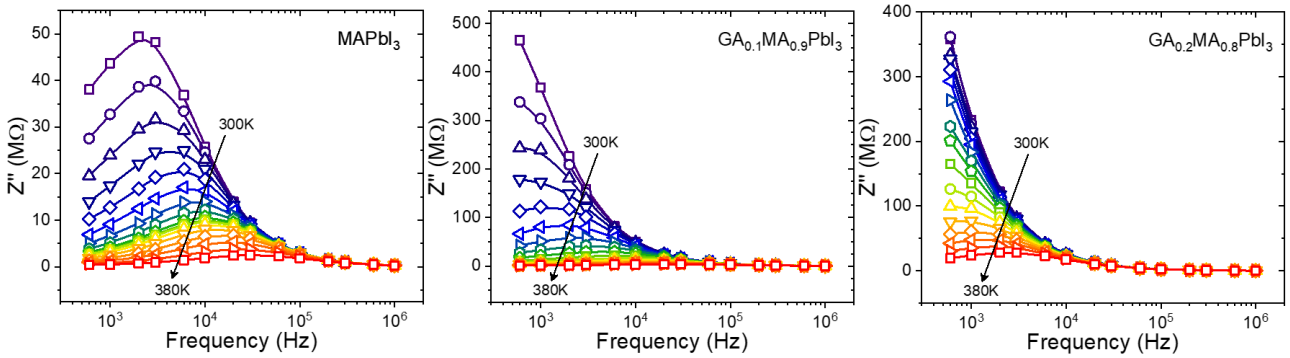

Fig. S11 - Dispersiont of imaginary part of the impedance of $GA_xMA_{1-x}PbI_3$ perovskites in the 600 Hz to 1 MHz and 300 to 380 K ranges. Lines are guides to the eyes.

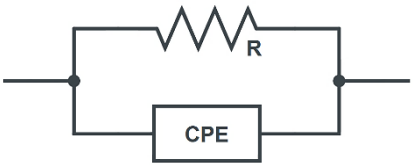

Fig. S12 - Illustration of a possible equivalent circuit representing the Cole-Cole model.

In the Cole-Cole model, it is assumed that the sample might be treated as a parallel association between a resistor of resistance R, and a CPE (constant phase element). In this case, the complex circuit impedance has the form given by:

$$Z^* = \frac{R}{1 + (i\omega\tau)^b}$$

where $\tau = 1/2\pi f_r$ is the mean relaxation time, f_r is the mean relaxation frequency, and b is the Cole-Cole coefficient, an empirical parameter, in the interval between 0 and 1, which reflects the existence

of a distribution of relaxation times in the material due to thermal fluctuations, structural inhomogeneities, etc. By using the Euler relation $i^b = cos(b\pi/2) + isin(b\pi/2)$, we get

$$Z^* = \frac{R}{1 + (\omega\tau)^b \left[cos\left(\frac{b\pi}{2}\right) + isin\left(\frac{b\pi}{2}\right)\right]} = \frac{R}{\left[1 + (\omega\tau)^b cos\left(\frac{b\pi}{2}\right)\right] + i\left[(\omega\tau)^b sin\left(\frac{b\pi}{2}\right)\right]}$$

Then, calling $\theta = {}^{b\pi}/_{2}$ and multiplying by the conjugate complex, it follows that

$$Z^* = \frac{R([1 + (\omega\tau)^b cos\theta] - i[(\omega\tau)^b sin\theta])}{[1 + (\omega\tau)^b cos\theta]^2 + [(\omega\tau)^b sin\theta]^2} = \frac{R([1 + (\omega\tau)^b cos\theta] - i[(\omega\tau)^b sin\theta])}{1 + 2(\omega\tau)^b cos\theta + [(\omega\tau)^b]^2}$$

Separating the real and imaginary components, it results

$$Z' = \frac{R + R(\omega\tau)^b cos\theta}{1 + 2(\omega\tau)^b cos\theta + [(\omega\tau)^b]^2}$$

$$Z'' = \frac{R(\omega\tau)^b sin\theta}{1 + 2(\omega\tau)^b cos\theta + [(\omega\tau)^b]^2}$$

Dividing Z'' by Z',

$$\frac{Z''}{Z'} = \frac{R(\omega\tau)^b sin\theta}{R + R(\omega\tau)^b cos\theta}$$

$$Z'' + Z''(\omega\tau)^b cos\theta - Z'(\omega\tau)^b sin\theta = 0$$

Now, isolating $(\omega\tau)^b$,

$$(\omega\tau)^b = \frac{Z''}{Z' sin\theta - Z'' cos\theta}$$

and substituing in Z'', it results

$$Z'' = \frac{Rsen\theta\left[\frac{Z''}{Z' sin\theta - Z'' cos\theta}\right]}{1 + 2cos\theta\left[\frac{Z''}{Z' sin\theta - Z'' cos\theta}\right] + \left[\frac{Z''}{Z' sin\theta - Z'' cos\theta}\right]^2}$$

$$1 + 2cos\theta\left[\frac{Z''}{Z' sin\theta - Z'' cos\theta}\right] + \left[\frac{Z''}{Z' sin\theta - Z'' cos\theta}\right]^2 = \frac{Rsin\theta}{Z' sin\theta - Z'' cos\theta}$$

Multiplying both sides by $[Z' sin\theta - Z'' cos\theta]^2$,

$$[Z' sin\theta - Z'' cos\theta]^2 + 2cos\theta Z''[Z' sin\theta - Z'' cos\theta] + Z''^2 = Rsin\theta[Z' sin\theta - Z'' cos\theta]$$

Performing quadratic and distributive operations,

$$Z'^2[sin\theta]^2 - 2Z''Z'[cos\theta sin\theta] + Z''^2[cos\theta]^2 + 2Z''Z'[cos\theta sin\theta] - 2Z''^2[cos\theta]^2 + Z''^2 = RZ'[sin\theta]^2 - RZ''[sin\theta cos\theta]$$

and canceling the opposite terms,

$$Z'^2[sin\theta]^2 - Z''^2[cos\theta]^2 + Z''^2 = RZ'[sin\theta]^2 - RZ''[sin\theta cos\theta]$$

it follows that

$$Z''^2(1 - [cos\theta]^2) + Z'^2[sin\theta]^2 + RZ''[sin\theta cos\theta] - RZ'[sin\theta]^2 = 0$$

Since $1-[cos\theta]^2=[sin\theta]^2$, hence

$$Z''^2[sin\theta]^2+Z'^2[sin\theta]^2+RZ''[sin\theta cos\theta]-RZ'[sin\theta]^2=0$$

and dividing this expression by $[sin\theta]^2$, it follows that

$$Z''^2+Z'^2+RZ''[cotg\theta]-RZ'=0$$

Adding $\left[\left({}^{R}/_{2}\right)cotg\theta\right]^2+\left({}^{R}/_{2}\right)^2$ on both sides of the equation and being $[cosec\theta]^2=1+[cotg\theta]^2$, we obtaing

$$\left[Z''+\frac{R}{2}cotg\theta\right]^2+\left[Z'-\frac{R}{2}\right]^2=\left[\frac{R}{2}cosec\theta\right]^2$$

which takes the form of an equation of radius circumference $\left({}^{R}/_{2}\right)cosec\theta$ centered in $\left[{}^{R}/_{2}\,,-\left({}^{R}/_{2}\right)cotg\theta\right]$. Finally, by isolating Z'', we get

$$Z''=\sqrt{\left[\frac{R}{2}cosec\left(\frac{b\pi}{2}\right)\right]^2-\left[Z'-\frac{R}{2}\right]^2}-\frac{R}{2}cotg\left(\frac{b\pi}{2}\right)$$

Thus, through an impedance Nyquist plot (Fig. S13), the fitting using this last expression provides the values of R and b. Then, considering the equation

$$\sigma=\frac{d}{aR}$$

where d is the sample thickness (Fig. S14), and a the electrode area, the conductivities of the samples of each material are calculated as a function of temperature. The obtained b values range from 0.75 to 0.97, depending on the composition and temperature (increasing GA^+ content and temperature reduces de b values found), thus deviating from the ideal Debye relaxation, ensuring the need to use the Cole-Cole model to fit our data.

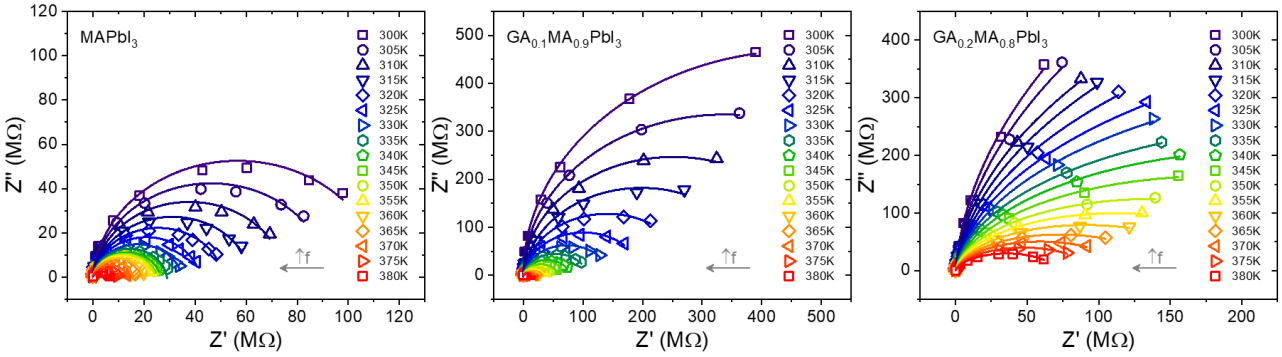

Fig. S13 - Impedance Nyquist plots of the $GA_xMA_{1-x}PbI_3$ samples. Hollow dots are the experimental data, and lines are the fits using the Cole-Cole derived expression.

Although laborious, we stress that the above procedure was necessary to obtain the desired parameters for a set of conditions where the relaxation frequencies could not be directly verified. The

fact that such relaxation frequencies are below the lower limit of the studied frequency range demonstrates that the relaxation times are long, indicating processes associated with ionic migration.

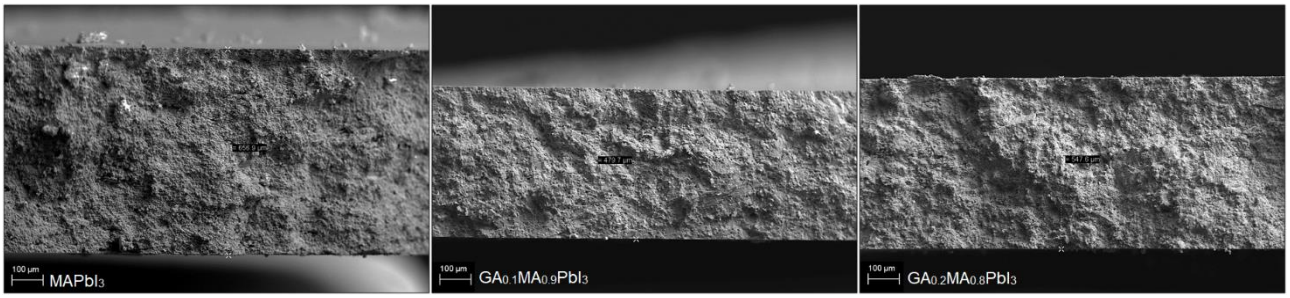

Fig. S14 - Cross-section SEM images of the $GA_xMA_{1-x}PbI_3$ samples used in the impedance measurements. Measured thicknesses are of about 657 µm, 480 µm, and 548 µm, respectively. Scale bar: 100 µm.

For halide perovskites, both ionic and electronic contributions for conductivity processes are expected. However, the latter can be considered less relevant for explaining the conductivities given the low relaxation frequencies observed in the impedance dispersions. Also, the fact that measurements are made in the dark and at moderate temperatures, sufficient to activate the migration of ions, but not so much to represent a large increase in the population of intrinsic carriers in materials with bandgaps of the order of 1.6 eV [5], much higher than the average thermal energy in the studied temperature range (k_BT ~ 0.03 eV). It is worth noting that point defect formation energies in $MAPbI_3$ are reported at values as low as 0.08 eV for I^- vacancies [24], well below the band gap energies. Thus, a high concentration of defects is expected, suggesting high ionic conductivity. Indeed, at 303 K, the ionic conductivity of the order of 1.2 x 10^{-6} S cm^{-1} is reported for $MAPbI_3$ single crystals, about two orders of magnitude higher than its electronic conductivity [25]. Also, it is reported that low iodine partial pressures (such as our measurements under vacuum conditions) favor ionic conductivity over electronic conductivity [26]. Taking everything into account, we argue that it is reasonable to assume that the electronic contribution to the conductivity found can be disregarded to explain our results.

Now, the associated relaxation time scales $\tau = RC$, where C is the sample (geometrical) capacitance, can be calculated with the relations $\sigma = d/aR$ and $C = \varepsilon'\varepsilon_0 a/d$. Putting all together,

$$\tau = \frac{d}{a\sigma}\frac{\varepsilon'\varepsilon_0 a}{d} = \frac{\varepsilon'\varepsilon_0}{\sigma}$$

which is a convenient form of the associated relaxation times in terms that represent the materials intrinsic properties. In the case here, ε' is the ε_∞ obtained in Supplementary Note 7. Using the above relation, we calculated the temperature variation of τ.

Finally, to confirm the calculation procedure, we obtained the relaxation frequencies of each composition over the studied temperature range. Results are given in the Fig. S15. The horizontal

dashed line is the lower impedance measurement frequency limit. Points below this line correspond to composition-temperature data for which a peak cannot be identified in the Nyquist plots. The comparison of results demonstrates that our methodology adequately describes the relaxation frequencies (times). Important to mention that the reduced relaxation frequency in the low frequency region (generally ascribed to the response of ion motion) upon guanidinium incorporation was previously found [27].

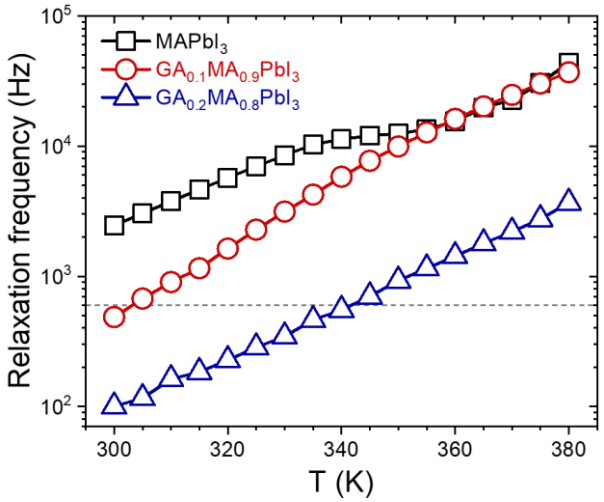

Fig. S15 - Calculated relaxation frequencies as a function of temperature for $GA_xMA_{1-x}PbI_3$ perovskites.

Supplementary Note 9: Insights from the ionic conductivity of $GA_xMA_{1-x}PbI_3$ perovskites

The ionic conductivity is given by $\sigma = qn_i\mu_i$, where q is the ion charge, n_i is the mobile ion (vacancy) density and μ_i the ion mobility [28]. It is well known that the formation of point defects, such as MA^+ and I^- vacancies, is guided by an increase in the configurational entropy [29]. The concentration of defects in the material is given by the balance between the increase in the configurational entropy and the enthalpy needed to create these defects. In mixed cation perovskites, the cation substitution should also contribute to the configurational entropy [30]. Hence, introducing an additional "source" of configurational entropy will affect the point defect concentration, decreasing it. In addition, the fact that the enthalpy formation of mixed cation systems, particularly with GA^+, is exothermic compared to pure $MAPbI_3$ [31] indicates that the enthalpy of defect formation in mixed systems is also higher, which contributes to the hypothesis of reduced defect concentration. An experimental result that corroborates this depicted scenario is that a lower density of traps in the $GA_{0.06}MA_{0.94}PbI_3$ composition was found compared to pure $MAPbI_3$ [32], given that electronic trap states can originate in point defects [33], which are also associated with electronic carrier recombination centers. In addition, a reduction on the defect density with increasing x up to 0.2 in the $FA_{1-x}Cs_xPbI_3$ system was observed [34]. Thus, the possible reduction in the vacancy concentration would explain, at least in part, the increase in the charge carrier lifetimes [4,7,35] and enhanced stabilities [1,5,36] observed in the literature for $GA_xMA_{1-x}PbI_3$ compositions.

Supplementary Note 10: I-V hysteresis

To evaluate the relation of the obtained parameters in the main text and the well-known current-voltage hysteresis, we measured the I-V curves for up and down electric potentials. Current versus voltage data were collected using a Keithley 6517B electrometer under dark conditions over several electrodes across the samples from -6 to 6 V with a 0.1 V s^{-1} scan rate. The difference between measured currents was plotted against the potential for each composition, and the resulting curves were integrated. Since the samples had different thicknesses (Fig. S14), we normalized the values to the geometric parameters of each sample by dividing the obtained areas by the product of the electrode area and the sample thicknesses. The resulting values have dimensions of energy per volume per time unit. We correlate this value to the energy dissipation difference between up and down curves, presumably due to the formation of forward and reversal ionic currents. The results are given in Fig. S16, from where we clearly see that the hysteresis value follows the same trend of the ionic conductivity as a function of GA^+-content, as expected from the most accepted interpretations for such phenomena [37]. Not surprisingly, we see the inverse correlation between the hysteresis and the relaxation times [38], here attributed to ionic charge carriers, which may be due to the faster accumulation of ions at electrodes, hindering the charge collection [39] and increasing the energy losses.

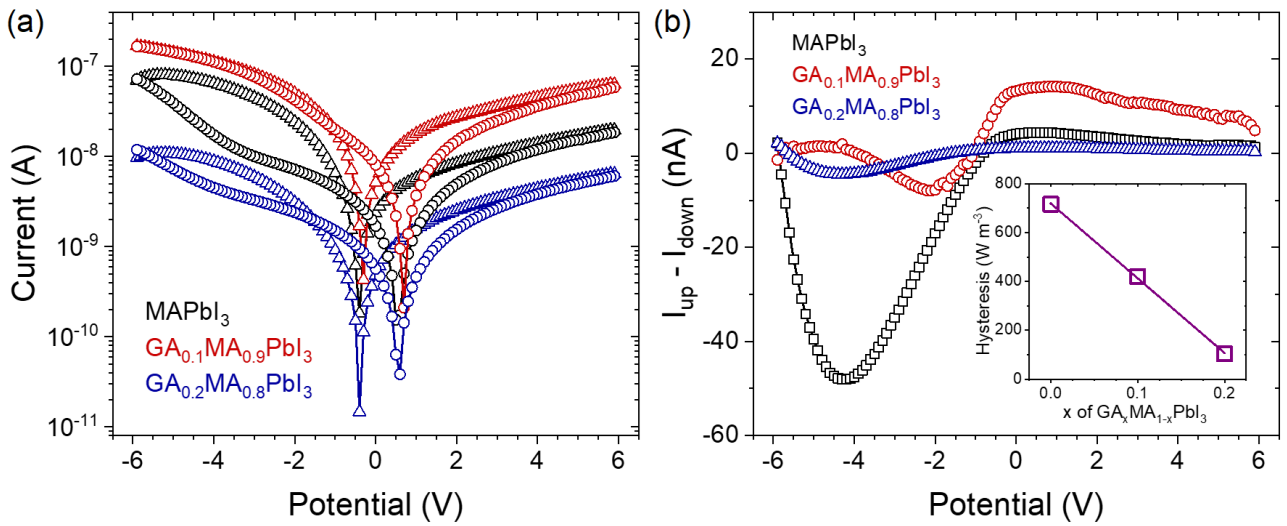

Fig. S16 - a) Up (triangles) and down (circles) current-potential curves for $GA_xMA_{1-x}PbI_3$ samples. The data shown are the mean values from nine measurements across the sample using different electrodes. The measurements were started at -6 V (up curves). b) Current difference between up and down curves as a function of potential. Inset shows the resulting hysteresis as a function of the guanidinium content.

Supplementary Note 11: Ionic migration activation energies in $GA_xMA_{1-x}PbI_3$

Table S4 - Comparison of ionic conductivity activation energies in $GA_xMA_{1-x}PbI_3$ compositions. Values are attributed to iodide ion migration.

Composition	E_a (eV)	Comment	Reference
$MAPbI_3$	0.37	Impedance spectroscopy in polycrystals	Present work
$GA_{0.1}MA_{0.9}PbI_3$	0.58		
$GA_{0.2}MA_{0.8}PbI_3$	0.47		
$MAPbI_3$	0.40	Impedance spectroscopy in thin-film solar cells; in $GA_{0.05}MA_{0.95}PbI_3$ the ion transport was too slow to be measured	[31]
$GA_{0.05}MA_{0.95}PbI_3$	-		
$MAPbI_3$	0.44	Ab initio simulations	
$GA_{0.25}MA_{0.75}PbI_3$	0.78		
$MAPbI_3$	0.52	Impedance spectroscopy in single crystals	[27]
$GA_{0.015}MA_{0.985}PbI_3$	0.37		
$MAPbI_3$	0.33	Temperature-dependent conductivity measurements in single crystals	[32]
$GA_{0.06}MA_{0.94}PbI_3$	0.59		

References

1 A. D. Jodlowski et al. *Nature Energy*, 2017, **2**, 972.

2 L. Dimesso et al. *Materials Science and Engineering: B*, **2016**, 204, 27.

3 N. Onoda-Yamamuro et al. *Journal of Physics and Chemistry of Solids*, 1990, **51**, 1383.

4 D. J. Kubicki et al. *Journal of the American Chemical Society*, 2018, **140**, 3345.

5 E. Vega et al. *Journal of Alloys and Compounds*, 2018, **739**, 1059.

6 S. Wu et al. *Chemical Communications*, 2019, **55**, 4315.

7 Y. Ding et al. *Journal of Energy Chemistry*, 2021, **58**, 48.

8 H. Park et al. *Machine Learning: Science and Technology*, 2021, **2**, 025030.

9 T. Haeger et al. *Journal of Materials Chemistry C*, 2020, **8**, 14289.

10 T. J. Jacobsson et al. *Inorganic Chemistry*, 2015, **54**, 10678.

11 P. Whitfield et al. *Scientific Reports*, 2017, **7**, 42831.

12 D. H. Fabini et al. *Angewandte Chemie International Edition*, 2016, **55**, 1.

13 O. J. Weber et al. *Journal of Materials Chemistry A*, 2016, **4**, 15375.

14 J. He et al. *ACS Energy Letters*, 2018, **3**, 2070.

15 A. Mohanty et al. *ACS Energy Letters*, 2019, **4**, 2045.

16 M. Simenas et al. *Nature Communications*, 2020, **11**, 5103.

17 J. M. Frost et al. *APL Materials*, 2014, **2**, 081506.

18 Z. Fan et al. *Journal of Physical Chemistry Letters*, 2015, **6**, 1155.

19 J. N. Wilson et al. *APL Materials*, 2019, **7**, 010901.

20 K. C. Kao. *Dielectric Phenomena in Solids*, Academic Press, 2004.

21 W. E. Vaughan. Dielectric relaxation. *Annual Review of Physical Chemistry*, 1979, **30**, 103.

22 K. Wang et al. *Journal of Physical Chemistry C*, 2021, **125**, 23050.

23 K. S. Cole and R. H. Cole. *Journal of Chemical Physics*, 1941, **9**, 341.

24 W. Ming et al. *Journal of Materials Chemistry A*, 2016, **4**, 16975.

25 W. Li et al. *Journal of Chemistry C*, 2020, **124**, 13348.

26 G. Y. Kim et al. *Advanced Functional Materials*, 2020, **30**, 2002426.

27 A. Mahapatra et al. *Physical Chemistry Chemical Physics*, 2020, *22*, 11467.

28 Moritz H. Futscher and Jovana V. Milić. *Frontiers in Energy Research*, 2021, **9**, 1.

29 A. Walsh et al. *Angewandte Chemie International Edition*, 2015, **54**, 1791.

30 Feray Ünlü et al. Chemical Processing of Mixed-Cation Hybrid Perovskites: Stabilizing Effects of Configurational Entropy. In: *Perovskite Solar Cells: Materials, Processes, and Devices*, 2022 Wiley-VCH GmbH.

31 D. W. Ferdani et al. *Energy and Environmental Science*, 2019, **12**, 2264.

32 WanFu Wang and Qiang Xu. *Nuclear Instruments and Methods in Physics Research Section A: Accelerators, Spectrometers, Detectors and Associated Equipment*, 2021, **1000**, 165234.

33 X. Qiu et al. *Nanoscale*, 2020, **12**, 22425.

34 Biwas Subedi et al. *Solar Energy Materials and Solar Cells*, 2018, **188**, 228.

35 N. de Marco et al. *Nano Letters*, 2016, **16**, 1009.

36 G. S. Kumar et al. *Nanoscale Horizons*, 2020, **5**, 696.

37 J.-W. Lee et al. *APL Materials*, 2019, **7**, 041111.

38 F. Ebadi et al. *Nature Communications*, 2019, **10**, 1574.

39 O. Almora et al. *Solar Energy Materials and Solar Cells*, 2019, **195**, 291.